Check for updates

Received: 4 April 2023 | Revised: 12 October 2023 | Accepted: 6 November 2023

DOI: 10.1002/qj.4618

Quarterly Journal of the Royal Meteorological Society RMetS

RESEARCH ARTICLE

Mid-level dry air intrusions over the southern Maritime Continent

Ashar A. Aslam[1] | **Juliane Schwendike**[1] | **Simon C. Peatman**[1] | **Cathryn E. Birch**[1] | **Massimo A. Bollasina**[2] | **Paul Barrett**[3]

[1]School of Earth and Environment, University of Leeds, Leeds, UK

[2]School of Geosciences, University of Edinburgh, Edinburgh, UK

[3]Met Office, Exeter, UK

Correspondence
Ashar A. Aslam, School of Earth and Environment, University of Leeds, Leeds, LS2 9JT, UK.
Email: eeaaas@leeds.ac.uk

Funding information
Natural Environment Research Council, Grant/Award Numbers: NE/T00039X/1, NE/R016739/1

Abstract

Patterns in extreme precipitation across the Maritime Continent in southeast Asia are known to be modulated by many processes, from large-scale modes of variability such as the Madden–Julian oscillation, to finer-scale mechanisms such as the diurnal cycle. Transient mid-level dry air intrusions are an example of a feature not extensively studied over the Maritime Continent, which has the potential to influence rainfall patterns. Here, we show that these dry air intrusions originate from upper level disturbances along the subtropical jet. Mid-level cyclonic circulation anomalies northwest of Australia from December to February (DJF) intensify westerlies in the southern Maritime Continent, advecting dry air eastward. In contrast, mid-level anticyclonic circulation anomalies northwest of Australia from June to August (JJA) intensify southern Maritime Continent easterlies, advecting dry air westward. The resultant transport direction of associated air parcels is also dependent on the seasonal low-level monsoon circulation. Dry air intrusions are important in influencing low-level wind and rainfall patterns, suppressing rainfall over seas near the southern Maritime Continent in both seasons, as well as over southern Maritime Continent islands in DJF and the Indian Ocean in JJA. In both seasons there is enhanced rainfall to the east of the intrusion, where there is moist return flow to the extratropics. This study highlights the importance of synoptic-scale extratropical features in influencing meteorological patterns in the Tropics.

KEYWORDS

deep convection, dry air intrusions, Maritime Continent, rainfall, tropical–extratropical interactions

1 | INTRODUCTION

The Maritime Continent (MC) in southeast Asia consists of an archipelago of thousands of islands and several shallow seas (Figure 1a). High sea-surface temperatures and variable topography make the region conducive to the formation of deep convection all year round. Rainfall over the MC (Figure 1b,c) is twice the global mean (Yamanaka et al., 2018), with mean precipitation rates exceeding 10 mm·day^{-1} (Ichikawa & Yasunari, 2006). The associated latent heat release influences the global atmospheric circulation and climate through Rossby wave generation and

This is an open access article under the terms of the Creative Commons Attribution License, which permits use, distribution and reproduction in any medium, provided the original work is properly cited.
© 2023 The Authors. *Quarterly Journal of the Royal Meteorological Society* published by John Wiley & Sons Ltd on behalf of the Royal Meteorological Society.

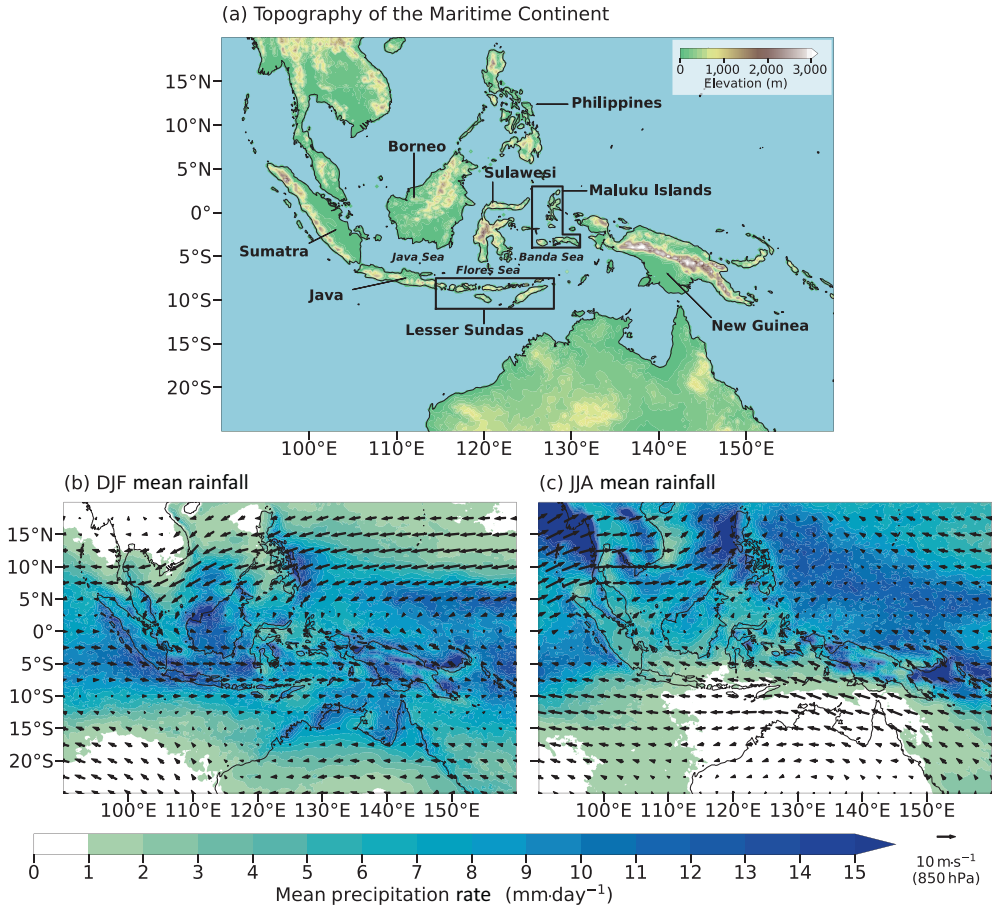

FIGURE 1 (a) Map showing the topography/elevation of the Maritime Continent, with some of its constituent islands and seas labelled. (b, c) The climatological means of Global Precipitation Measurement precipitation rates for (b) December 2000–February 2001 to December 2019–February 2020 (DJF) and (c) June–August 2001 to June–August 2020 (JJA). Black arrows represent 850 hPa wind.

subsequent propagation towards the extratropics (Jin & Hoskins, 1995). The MC has therefore been termed an "atmospheric boiler box" (Ramage, 1968).

Deep convection over the MC encompasses multiple spatial and temporal scales, and several mechanisms modulate precipitation patterns. These processes include the diurnal cycle of solar heating (e.g., Mori et al., 2004; Qian, 2008; Yokoi et al., 2017), large-scale modes of variability such as the Madden–Julian Oscillation (MJO; e.g., Madden & Julian, 1971; Madden & Julian, 1972; Madden & Julian, 1994), El Niño–Southern Oscillation (ENSO; e.g., Haylock & McBride, 2001), the Indian Ocean Dipole (IOD; e.g., Saji et al., 1999; Saji & Yamagata, 2003), and equatorial waves (e.g., Wheeler & Kiladis, 1999; Yang et al., 2003; Ferrett et al., 2020). Scale interactions also exist between processes, adding further variability, and therefore complexity, to our understanding of convective organisation, water vapour profiles, and cloud structure over the MC (e.g., Rauniyar & Walsh, 2013; Peatman et al., 2014; Peatman et al., 2021). Limitations in our knowledge of these mechanisms lead to errors in model-simulated precipitation patterns over the MC, primarily due to issues in resolving finer scale features, or because of the parametrisation design (e.g., Yang & Slingo, 2001; Neale & Slingo, 2003; Qian, 2008; Birch et al., 2016; Vincent & Lane, 2016).

Another feature with the potential to influence regional precipitation patterns is a dry air intrusion (DAI), which is a descending tongue of low specific, and relative, humidity and high potential vorticity (PV), hundreds of kilometres in width, injected from the upper troposphere/lower stratosphere (Appenzeller & Davies, 1992; Browning, 1997; Danielsen, 1968). Extratropical wave trains act as a source of DAIs, as shown by back trajectory analysis (e.g., Casey et al., 2009) and neural networks (Silverman et al., 2021). Amplification of disturbances along the upper level subtropical jet leads to isentropic folding of the tropopause and anticyclonic Rossby wave breaking, forcing descent of upper level dry air (Bithell et al., 1999; Funatsu & Waugh, 2008; Numaguti, 1995). The resultant direction that dry air is transported depends on factors such as the jet position and the background wind field (Homeyer & Bowman, 2013).

The frequency of DAI events has large spatial variability. Waugh and Polvani (2000), Stohl (2001), Casey et al. (2009), and Raveh-Rubin (2017) produced climatologies of DAI occurrence (the latter two offering global coverage). DAIs are most prevalent over the Pacific and Indian oceans, occurring more often in the winter season for each hemisphere. However, they contribute to anomalously dry air all year round.

1477870x, 2024, 759, Downloaded from https://rmets.onlinelibrary.wiley.com/doi/10.1002/qj.4618 by Test, Wiley Online Library on [21/03/2024]. See the Terms and Conditions (https://onlinelibrary.wiley.com/terms-and-conditions) on Wiley Online Library for rules of use; OA articles are governed by the applicable Creative Commons License

Atmospheric soundings show DAIs sit atop sharp stable layers, produced by anomalous long-wave cooling of the top of the underlying moist air (Johnson et al., 2001; Mapes & Zuidema, 1996; Zhang & Chou, 1999). The radiative and convective profile in the Tropics can therefore be perturbed by humidity fluctuations attributed to DAIs coming from the extratropics (Brown & Zhang, 1997; Ryoo et al., 2008). Such disturbances can affect the moisture field and the low-latitude circulation, thereby impacting regional meteorology and environmental conditions (e.g., Rodwell, 1997; Knippertz, 2007).

Localised, transient breaks in tropical precipitation on daily-to-weekly time-scales can be associated with DAIs. This link has been observed in regions such as the tropical West Pacific during the Tropical Ocean Global Atmosphere Coupled Ocean–Atmosphere Response Experiment (TOGA COARE; e.g., Mapes & Zuidema, 1996; Yoneyama & Parsons, 1999; Lucas & Zipser, 2000; Lucas et al., 2000; Parsons et al., 2000) and the Indian subcontinent, such as through the Interaction of Monsoon Precipitation and Convective Organization, Atmosphere, Surface and Sea project (INCOMPASS; e.g., Parker et al., 2016; Fletcher et al., 2020; Volonté et al., 2020).

Mid-level DAIs cap the moist boundary layer, decreasing boundary-layer parcel buoyancy and increasing convective inhibition. Gradual increases in boundary-layer equivalent potential temperature and potential instability lead to convective available potential energy build-up (Brown & Zhang, 1997; Parker et al., 2016; Yang et al., 2009). Increases in convective available potential energy allow convection to erode the dry air layer, primarily through convective cloud detrainment. Convective recovery is, however, non-steady, being influenced by both local factors (e.g., the diurnal cycle, orography, convective structure, and surface feedbacks) and remote factors (including synoptic circulations and dynamics originating from the extratropics) (Brown & Zhang, 1997; Fletcher et al., 2018; Mapes & Zuidema, 1996; Redelsperger et al., 2002; Volonté et al., 2020).

DAIs can also result in low-level convergence, vertical motion, and increased convection when encountering warm, moist air masses on eastward margins and leading edges, through isentropic displacement and reductions in potential stability ahead of upper-level troughs (e.g., Funatsu & Waugh, 2008; Vaughan et al., 2017). Disturbances along the jet stream and their resultant DAIs can therefore steer and organise deep convection, through which increases in rainfall may be observed (Allen et al., 2009; Berry & Reeder, 2016). However, the environment near to the intrusion must be moist enough to be conducive to the formation of deep convection (de Vries et al., 2016; de Vries et al., 2018; Kumar et al., 2019). As DAIs themselves modify the lower-level wind field, they can therefore enhance the moisture flux enabling convection downstream (Knippertz, 2007; Rodwell, 1997; Ward et al., 2021).

Despite insights gained from previous studies across the Tropics, DAIs have not been extensively studied in relation to MC precipitation. Murata et al. (2006) and Seto et al. (2006) used rawinsonde, radar, and surface meteorological data and identified DAIs over Sumatra. Murata et al. (2006) noted events where there is convective suppression behind eastward-propagating squall lines. Seto et al. (2006) found this suppression to be associated with intensification of westerly winds. More recently, Feng et al. (2021) used the Sumatran Global Positioning System array to investigate summer intraseasonal variability in precipitable water vapour, a property that influences the propagation of the satellite signal. DAIs over Sumatra were associated with interactions linked to Rossby waves propagating in the Southern Hemisphere midlatitudes. However, these studies use a small number of events in their analysis and do not explicitly analyse impacts on rainfall in the region.

Rodwell (1997) highlighted that limits to the accuracy of seasonal forecasts and predictability of rainfall can be influenced by synoptic-scale/transient events such as DAIs, particularly if a single event provides significant contributions to the seasonal anomaly. Anomalies associated with DAIs could represent a significant challenge for accurate seasonal forecasts as the slowly varying lower boundary conditions, evolving from initial conditions, cannot anticipate transient events such as DAIs. Further research into processes regulating regional precipitation will benefit society in the MC, as communities experience serious floods and landslides as a result of extreme weather. Better meteorological understanding will improve forecasting potential and ensure socioeconomic security for the 500 million people living in the MC, alleviating current vulnerability to disaster and loss (Narulita & Ningrum, 2018; Wijayanti et al., 2017).

In this study, we aim to identify mechanisms that enable the occurrence of DAIs and their impact on rainfall over the southern MC and to establish any seasonal differences. We use 42 years of European Centre for Medium-Range Weather Forecasts Reanalysis v5 (ERA5) data to identify dry events near the MC through analysis of variance and anomalies in humidity. Section 2 outlines the methods used, including the data utilised, the choice of study location, the workflow in identifying dry events, and computation of air parcel trajectories to determine attribution to DAIs. We present the results in Section 3, including parcel trajectories, regulatory mechanisms of mid-level dry events, and impacts on regional rainfall patterns. Section 4 synthesises these results to see whether

1477870x, 2024, 759, Downloaded from https://rmets.onlinelibrary.wiley.com/doi/10.1002/qj.4618 by Test, Wiley Online Library on [21/03/2024]. See the Terms and Conditions (https://onlinelibrary.wiley.com/terms-and-conditions) on Wiley Online Library for rules of use; OA articles are governed by the applicable Creative Commons License

there are similarities between this work and past studies, or whether processes and impacts related to dry events are unique for this region. Conclusions are provided in Section 5.

2 | METHODS

2.1 | Data

ERA5 data of global climate and weather (Hersbach et al., 2020) are used to investigate DAIs. Instantaneous hourly ERA5 data (at a horizontal grid spacing of 0.25° × 0.25°, equivalent to 26 km) from 1979 to 2021 (42 years) were used. Data were used for 20 levels from 50 hPa to 1,000 hPa at 50 hPa vertical resolution, for the domain of 20° N–60° S, 60°–160° E. The hourly data were then used to determine daily means for each variable across the domain. Daily mean rainfall data from the Global Precipitation Measurement (GPM) mission, preprocessed using the Integrated Multi-Satellite Retrievals for GPM (IMERG) Version 06 algorithm (Huffman et al., 2020), were also used. The IMERG algorithm inter-calibrates gauge data with precipitation estimates from satellite infrared and microwave sensors. GPM data were available at 0.1° × 0.1° horizontal grid spacing, for 20 years from December 2000 to November 2020.

Daily means were averaged over all years for each variable to produce a climatological mean daily annual cycle, which was later smoothed using a 30-day mean.

2.2 | Dry event identification

The analysis of the variance in daily mean specific humidity at 700 hPa was conducted for each season, in order to identify regions exhibiting fluctuations in mid-level humidity. A box was selected based on the spatial pattern of the variance. As shown in Figure 2a, the highest variance in mid-level specific humidity is observed either side of the MC. Prominent locations of high variance include the eastern Indian Ocean southwest of Sumatra and Java, and the southwestern tropical Pacific Ocean near New Guinea and Australia. A box was selected covering the region of 9°–20° S, 95°–115° E, near to Sumatra and Java. This box encloses the eastern periphery of the first high-variance region identified, located between 10°–20° S and 80°–100° E.

The method of identifying dry events presented is illustrated schematically in Figure 2b. Anomalies in 700 hPa daily mean specific humidity were first calculated relative to the associated days and months within the smoothed mean annual cycle, averaged over the identifier box. These anomalies were then normalised by dividing by that same day within the smoothed mean annual cycle. Dry days were defined as days where normalised specific humidity anomalies are below the fifth percentile, computed for each season from 1979–80 to 2020–21. If a dry day has a normalised specific humidity anomaly more negative than the 10 days preceding and following it, the dry day represents the middle, or "day 0", of a dry event, which is a local humidity minimum. This method is chosen so that events associated with an individual DAI are isolated, ensuring they are not accounted for more than once. Effects of DAIs are noted up to 8–15 days after an intrusion (in TOGA COARE; e.g., Yoneyama & Fujitani, 1995; Parsons et al., 2000), so defining events with a 10-day window either side of a minimum in normalised specific humidity anomalies can be justified.

2.3 | Trajectory analysis

A Lagrangian trajectory analysis is used to track air parcels associated with dry events. Advection of each parcel only requires details of the three-dimensional wind field, used to track the location and physical properties of these particular parcels for time periods of interest. Trajectories were calculated by determining a first guess (denoted with a prime symbol) position of a parcel at time $t + \Delta t$, given by

$$\mathbf{r}'_{t+\Delta t} = \mathbf{r}_t + \mathbf{v}_t(\mathbf{r}_t) \cdot \Delta t, \tag{1}$$

where $\mathbf{r}$ is the three-dimensional spatial coordinate of the air parcel, and $\mathbf{v}$ is the three-dimensional wind velocity field at position $\mathbf{r}$ (e.g., Wernli & Davies, 1997; Draxler et al., 1998). Δt represents the time step, which is 1 day for forward trajectory analysis and −1 day for back trajectory analysis. An adjusted mean wind is determined from

$$\overline{\mathbf{v}} = 0.5[\mathbf{v}_t(\mathbf{r}_t) + \mathbf{v}_{t+\Delta t}(\mathbf{r}'_{t+\Delta t})], \tag{2}$$

to give the final position of the air parcel

$$\mathbf{r}_{t+\Delta t} = \mathbf{r}_t + \overline{\mathbf{v}} \cdot \Delta t. \tag{3}$$

Trajectories were computed for each grid point within the identifier box (9°–20° S, 95°–115° E) at day 0, where both latitude and longitude co-ordinates are integers (12 × 21 points). As ERA5 data is at 0.25° horizontal resolution, and data is downloaded at 50 hPa vertical resolution, when a guess position is not located on these defined grid points or levels, tri-linear interpolation is applied to determine the values of $\mathbf{v}$ associated with their position $\mathbf{r}$. If $\mathbf{r}$ exists outside the domain (20° N–60° S, 60°–160° E, for vertical pressure levels between 50 and 1,000 hPa), the

1477870x, 2024, 759, Downloaded from https://rmets.onlinelibrary.wiley.com/doi/10.1002/qj.4618 by Test, Wiley Online Library on [21/03/2024]. See the Terms and Conditions (https://onlinelibrary.wiley.com/terms-and-conditions) on Wiley Online Library for rules of use; OA articles are governed by the applicable Creative Commons License

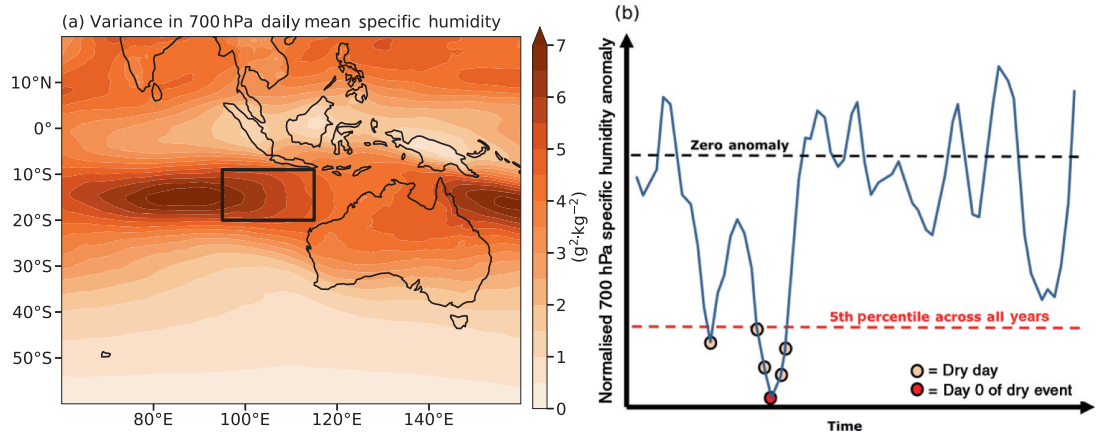

FIGURE 2 (a) Variance in daily mean specific humidity at 700 hPa for the entire time period of analysis from December 1979 to November 2021. The black box (9°–20° S, 95°–115° E) represents the selected region in this study for identification of mid-level dry events. (b) An illustration of the method described for identifying dry events. The soild line is a time series of normalised 700 hPa specific humidity anomalies for a particular season and year. The top dashed line represents zero anomaly, and the bottom dashed line represents the fifth percentile of normalised 700 hPa specific humidity anomalies as calculated across all 42 years for a particular season. Paler dots represent dry days, and darker dots represent day 0 of dry events, where the anomaly is at its most negative relative to neighbouring days.

trajectory is terminated. We find that using a daily-mean wind input does not fundamentally change the mean trajectory path compared with using an hourly input (not shown).

2.4 | Association with modes of variability

Dry events were grouped into associations with the phases of ENSO, IOD, and MJO to determine associations between dry events and larger scale controls. Details on the data representing these modes of variability can be found in Table1. Ratios were calculated from the frequencies of these events by dividing the fraction of events in each phase relative to the total number of events per season by the fraction of days in each phase relative to the total number of days in each season across the 42 years. This calculation provides a ratio between event frequency and day frequency with respect to each phase. If this ratio equals 1, the phase is as likely to occur during dry events as it is all days. If the ratio is 2, then the phase is twice as likely to occur during dry events.

Statistical significance of links between dry event occurrence and large-scale modes of variability was tested through bootstrapping. For each season, we randomly subset a set of days of equivalent length to the number of events identified per season, where the state of each mode for each day is determined. We perform the calculations of ratios as described previously for these sets of days, relative to the distribution of days in the whole season across the phases of each mode. This process is repeated 1,000 times to produce a distribution of ratios for the state of each mode for each season. Percentiles for the original ratios relative to the bootstrapped distribution are then calculated. These percentiles allow the determination of the significance of association with modes of variability relative to a selected confidence interval.

3 | RESULTS

This section outlines the results obtained from this study. Section 3.1 provides details on the number of dry events identified, outcomes from parcel trajectory analysis for case studies, and for all dry events. Section 3.2 seeks to provide reasoning for such trajectories through understanding mechanisms regulating the occurrence of dry events. Statistical links between dry event occurrence and phases of various modes of variability are provided in Section 3.3. Lastly, Section 3.4 shows the results in analysing changes to rainfall patterns during dry events.

3.1 | Dry event characteristics and parcel trajectories

Employing the chosen method described in Section 2.2, we identify 201 dry events over the 42-year period of analysis. Focusing on December–February (DJF) and June–August (JJA), we find 47 and 56 dry events respectively, equivalent to just over one event per season per year.

1477870x, 2024, 759, Downloaded from https://rmets.onlinelibrary.wiley.com/doi/10.1002/qj.4618 by Test, Wiley Online Library on [21/03/2024]. See the Terms and Conditions (https://onlinelibrary.wiley.com/terms-and-conditions) on Wiley Online Library for rules of use; OA articles are governed by the applicable Creative Commons License

TABLE 1 The indices (their derivations and the definitions of events related to the various modes) used in analysing links between the states of selected modes of variability and the occurrence of dry events[a].

Mode	Index and derivation	Event definition
ENSO	Monthly ONI (NOAA, 2019), derived from the average temperature anomaly in the surface waters of the central-eastern tropical Pacific.	El Niño events are defined where ONI $\geqslant 0.5$°C for five successive months, and La Niña events are defined where ONI $\leqslant -0.5$°C for five successive months.
IOD	Monthly Indian Ocean DMI (Saji & Yamagata, 2003), derived from the anomalous sea-surface temperature gradient between the the western equatorial and southeastern equatorial Indian Ocean.	Positive IOD events are defined where DMI $\geqslant 0.4$°C for three successive months. Negative IOD events are defined where DMI $\leqslant -0.4$°C for three successive months.
MJO	Daily real-time multivariate MJO series 1 and 2 (RMM1 and RMM2), the principal components of the two leading EOFs, defined by EOF analysis of the combined field of outgoing long-wave radiation and wind, which define the phase of the MJO (Wheeler & Hendon, 2004). The amplitude is defined as $\sqrt{\text{RMM1}^2 + \text{RMM2}^2}$.	MJO events occur when the amplitude for a specific day $\geqslant 1$. Where the MJO amplitude is <1, we label an event as being under "phase 0".

Note: The sources for the indices are noted in the Acknowledgements.
Abbreviations: DMI, dipole mode index; ENSO, El Niño–Southern Oscillation; EOF, empirical orthogonal function; IOD, Indian Ocean Dipole; MJO, Madden–Julian Oscillation; ONI, Ocean Niño Index.

We first analyse where air parcels associated with identified dry events originate from and are advected to, using the parcel trajectory equations provided in Section 2.3. Initial analysis is performed on select events, and Figure 3 shows results for events that had normalised specific humidity anomalies equivalent to the event-average per season. These are the January 9, 2020 (Figure 3a–c), and July 26, 2020 (Figure 3d–f), dry events for DJF and JJA respectively.

Back trajectory analysis shows that air parcels associated with the selected DJF dry event originate largely from the extratropics in the southeast Indian Ocean (30°–50° S), 6–9 days prior to the peak of the dry event (Figure 3a), descending from 200 to 500 hPa (Figure 3c). Forward trajectories show that, on average, air parcels remain confined within near-equatorial latitudes from 5° to 20° S (Figure 3b), descending further to the near surface for up to 10 days after the peak of the dry event before reascending to upper levels (Figure 3c). Some parcels, however, ascend rapidly just after day 0. Most air parcels are advected eastward towards New Guinea and northern Australia in the southeast, with a slightly smaller portion westward towards the Indian Ocean. Some trajectories recurve back towards the Southern Hemisphere extratropics.

For the selected JJA dry event, air parcels largely originate from the extratropics as well, though slightly further north than in DJF, between 20° and 40° S, in the southeastern Indian Ocean 3–6 days prior to the peak of the dry event (Figure 3d), descending from the upper levels between 300 and 500 hPa (Figure 3f). An additional (albeit much smaller) source of air parcels is located over the Tropics around New Guinea and the western Pacific, up to 12 days prior to the peak. Forward trajectories show that most air parcels are advected towards the eastern Indian Ocean, within 6 days of the peak (Figure 3e). After this, up to 15 days after the peak of the dry event, many trajectories are directed northeastward towards mainland southeast Asia and the northern MC. Few trajectories return to the extratropics to the south of Australia. On average, air parcels continue descending in some cases beyond 10 days after the peak of the dry event (Figure 3f).

Figure 4 shows the distribution of air parcels associated with all dry events in DJF and JJA, to corroborate the aforementioned analysis based on individual events. Solid contours represent the limits of the trajectory to the number of days listed above the figure panels for DJF and JJA. Filled contours represent the difference between these distributions, where positive (negative) values represent where more DJF (JJA) air parcels are located. The JJA distribution is rescaled to have the same number of parcel trajectories as DJF, by multiplying the distribution in JJA by the number of events in DJF (47), divided by the number in JJA (56).

At 10–15 days before the event, JJA parcels are located further to the north of the MC between 0° and 15° S and 80°–160° E, whereas DJF parcels are located further south over the Indian Ocean between 15°–35° S and 60°–130° E. (Figure 4a). Going forward in time, average trajectories suggest parcels most commonly enter the domain from the upper troposphere between 200 and 500 hPa (Figure 4g) and extratropics over the southern Indian Ocean to the west (Figure 4b). This is observed most strongly during DJF 5–10 days before the peak of the dry event, but also in JJA. Just before the peak of the dry event, most DJF

1477870x, 2024, 759, Downloaded from https://rmets.onlinelibrary.wiley.com/doi/10.1002/qj.4618 by Test, Wiley Online Library on [21/03/2024]. See the Terms and Conditions (https://onlinelibrary.wiley.com/terms-and-conditions) on Wiley Online Library for rules of use; OA articles are governed by the applicable Creative Commons License

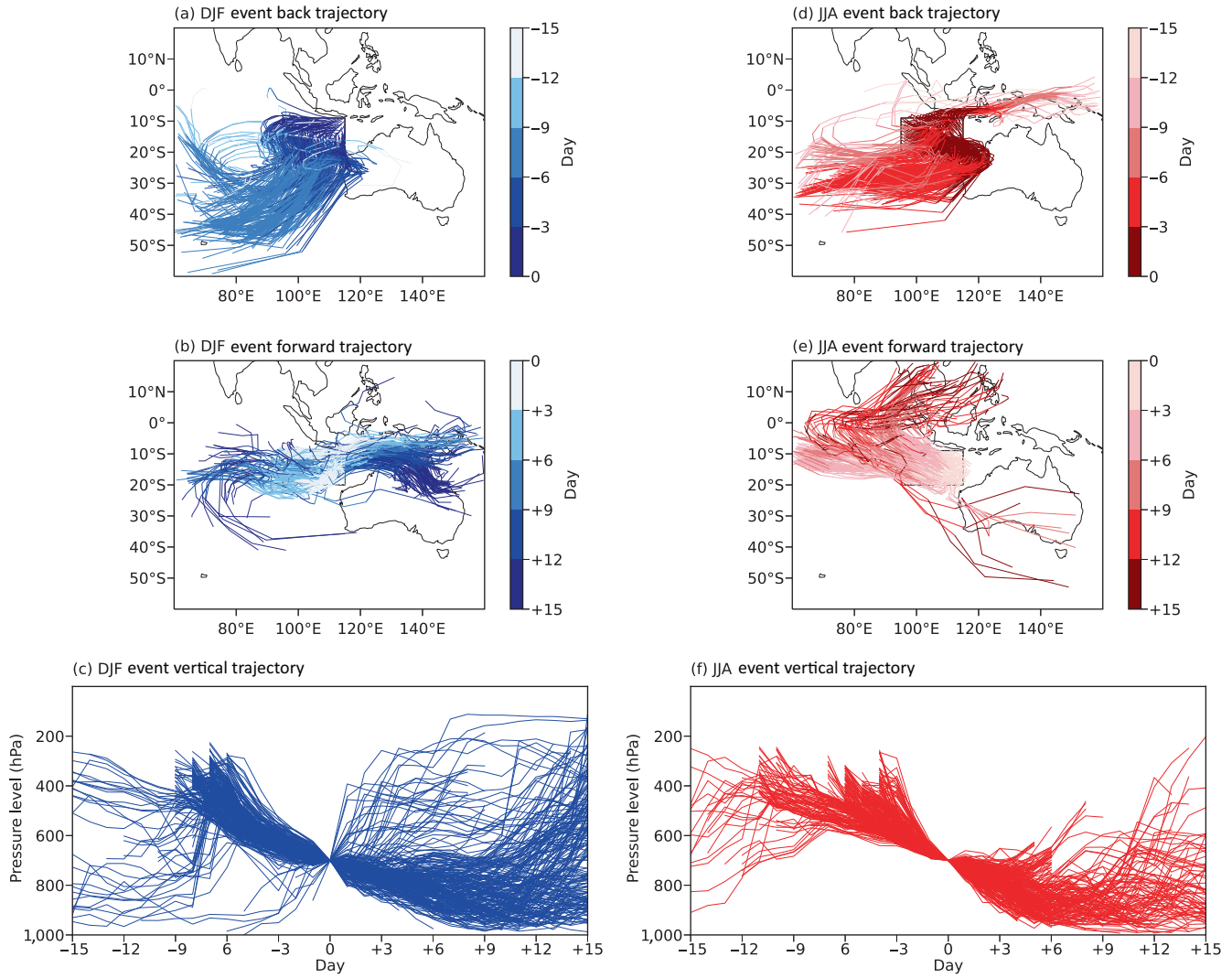

FIGURE 3 Air parcel trajectories for the (a–c) January 9, 2020, December–February (DJF) and (d–f) July 26, 2020, June–August (JJA) dry events: (a, d) back, (b, e) forward, and (c, f) vertical trajectories.

parcels are close to the identifier box where trajectories began (Figure 4c). However, the JJA distribution suggests parcels can come from the extratropics during the 5 days before the event peak, with some advected southwestward from the Tropics. The extratropical source to the southwest is, however, common to both DJF and JJA regardless of how far back in time one goes, though JJA has an additional (yet smaller) source coming from the Tropics east of New Guinea.

Up to 5 days after the dry event peak, DJF parcels are mostly advected eastward across the MC towards New Guinea, with some also advected westward (Figure 4d). Up to 10 days after the event, the eastward propagation noted in DJF persists (Figure 4e). Compared with DJF, JJA parcels are, on average, advected northwest towards India, but some are also advected northeastward over Sumatra and Malaysia towards mainland southeast Asia (Figure 4d–f).

Air parcels associated with the trajectories linked to dry events have a characteristic descent from 10 days before the event peak to 10 days after (Figure 4g). However, DJF parcels, compared with JJA, originate from the upper levels further back in time, taking longer to descend to the mid-levels. After the event, JJA parcels have a stronger descent signal than DJF parcels do, which has a broader vertical distribution, linked to an increase in the number of parcels that end up reascending to the upper levels.

3.2 | Regulatory mechanisms

Here, we provide insight into mechanisms regulating dry event occurrence for events identified in DJF and JJA. Figures 5 and 6 show lead–lag composites of specific humidity anomalies for DJF and JJA events.

1477870x, 2024, 759, Downloaded from https://rmets.onlinelibrary.wiley.com/doi/10.1002/qj.4618 by Test, Wiley Online Library on [21/03/2024]. See the Terms and Conditions (https://onlinelibrary.wiley.com/terms-and-conditions) on Wiley Online Library for rules of use; OA articles are governed by the applicable Creative Commons License

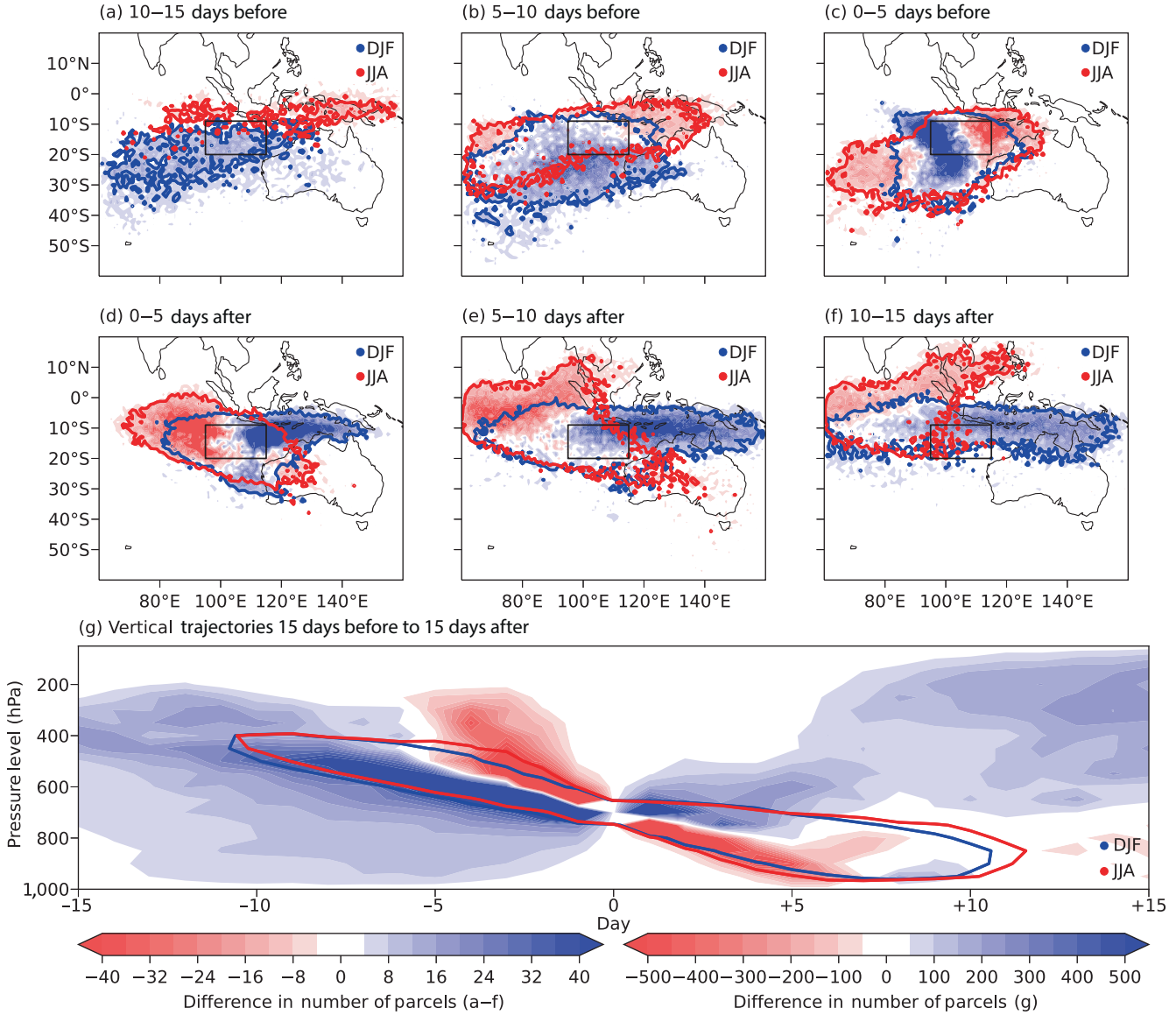

FIGURE 4 The distribution in dry-event-related air parcels as calculated through (a–c) back and (d–f) forward trajectory analysis. Solid contours represent the limits of the trajectory to the number of days listed above the figure panels for December–February (DJF) and June–August (JJA). This is indicated by contours where the sum of parcels across the days, labelled above the figure panels, is 10 parcels. Filled contours represent differences between the distribution in each season, where the difference is the JJA distribution subtracted from the DJF distribution, where the JJA distribution is rescaled to have the same number of parcel trajectories as DJF, done by multiplying the distribution in JJA by the number of events in DJF (47), divided by the number in JJA (56). This rescaling allows a difference between JJA and DJF to be calculated (otherwise there will be a tendency for differences to shift towards the negative with more parcels present in the domain in JJA than DJF, by virtue of the difference in number of events). (g) The distributions for each season as a function of time and vertical pressure level, summed over all longitudes and latitudes. Solid contours represent the limits of the vertical trajectory to the day labelled on the *x*-axis for DJF and JJA. These limits are indicated by contours, where the sum of parcels is 1,000 parcels.

During DJF, up to 7 days before the peak of the dry event, a moist anomaly develops over northern Australia (Figure 5a). Mid-level westerly anomalies form over the southern MC, with a mid-level cyclonic circulation anomaly developing northwest of Australia. Between days −4 and −2, a dry anomaly south of the MC evolves, driven by southerly advection from the extratropics (Figure 5b). At upper levels, this advection is linked to disturbances along the subtropical jet, where a cyclonic circulation anomaly develops southwest of Australia, bounded by anticyclonic circulation anomalies either side. Mid-level circulation anomalies almost parallel those at the upper levels, extending further northward towards the MC. Westerlies over the southern MC are enhanced, and the

1477870x, 2024, 759, Downloaded from https://rmets.onlinelibrary.wiley.com/doi/10.1002/qj.4618 by Test, Wiley Online Library on [21/03/2024]. See the Terms and Conditions (https://onlinelibrary.wiley.com/terms-and-conditions) on Wiley Online Library for rules of use; OA articles are governed by the applicable Creative Commons License

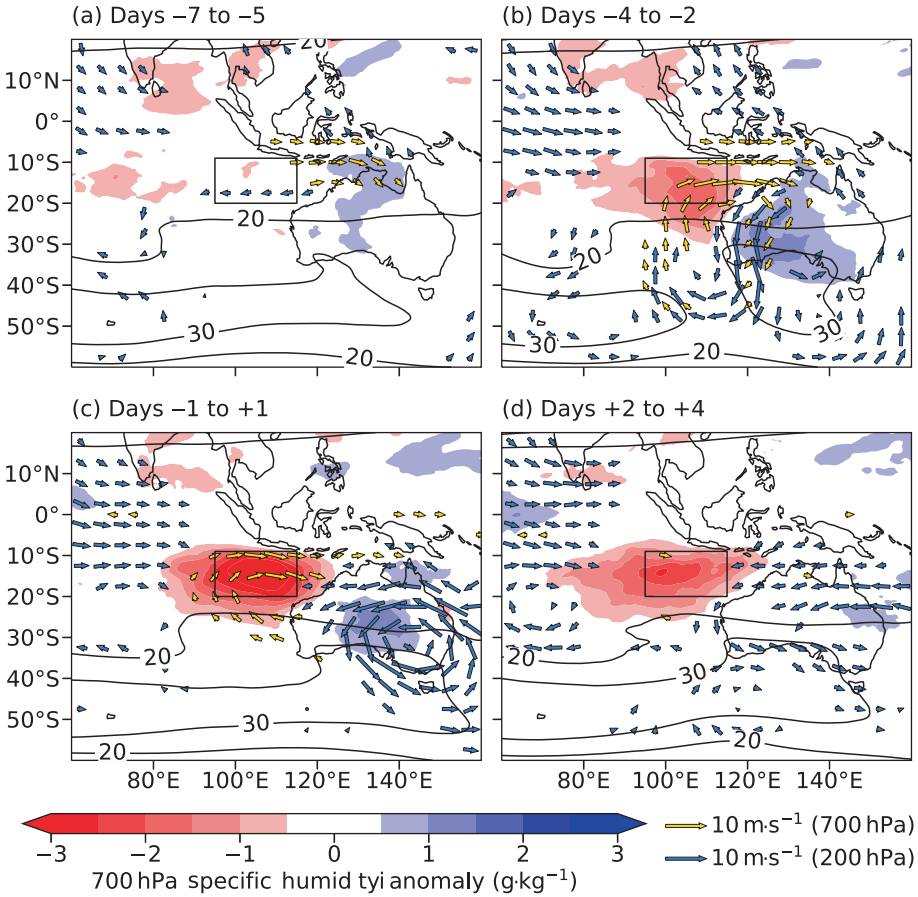

FIGURE 5 Lead–lag composites for 700 hPa specific humidity anomalies for the 47 dry events identified in December–February (DJF) from 1979–80 to 2020–21 for (a) days −7 to −5, (b) days −4 to −2, (c) days −1 to +1, and (d) days +2 to +4. Paler and darker arrows represent composite 700 hPa and 200 hPa anomalous wind respectively, calculated as the average of wind anomalies for each event relative to the DJF mean annual cycle. Anomalous wind at each level less than 2 $m \cdot s^{-1}$ is not shown. Solid contours represent 200 hPa wind speed at 20 $m \cdot s^{-1}$ and 30 $m \cdot s^{-1}$, indicating the position of the DJF subtropical upper level jet. The black box represents the domain used for identifying dry events as in Figure 2.

intensified return flow to the extratropics east of the mid-level cyclonic anomaly increases the moist anomaly over Australia.

Around day 0, while the dry anomaly intensifies, upper level disturbances in the extratropics dissipate (Figure 5c). However, the anticyclonic circulation anomaly over Australia persists, resulting in a preserved moist anomaly there. The mid-level cyclonic circulation anomaly near the MC develops a northwest–southeast tilt, centred just off northwestern Australia, and the previously enhanced westerlies begin to weaken. Between days +2 and +4, the dry anomaly begins to dissipate and spreads out longitudinally, with the moist anomaly over Australia also reduced (Figure 5d). Anomalous mid-level westerlies in the southern MC are weaker than prior to the dry event peak, linked to the weakened mid-level cyclonic anomaly.

For JJA, between days −7 and −5, a dry anomaly forms to the east over northern Australia and seas adjacent to MC islands (Figure 6a). This anomaly stems from upper level disturbances further east over eastern Australia, with southeasterly advection towards the MC. However, composite mid-level wind anomalies here are weak. The pre-existing dry air migrates westward over Java, the Lesser Sundas, South Sulawesi, the Maluku Islands, and neighbouring seas (Java and Flores; Figure 1a) between days −4 and −2 (Figure 6b). A new upper level disturbance develops to the southwest of the selected box over the southeastern Indian Ocean, leading to southerly-to-southeasterly advection at the upper levels. This advection is linked to an anticyclonic circulation anomaly, intensifying easterlies at mid-levels to the west of the MC, as well as dry air advection into the Tropics.

Around day 0, strong upper level anticyclonic and cyclonic circulation anomalies are observed to the west and over Australia respectively (Figure 6c). A mid-level anticyclonic circulation anomaly extends into the Tropics, increasing the intensity of the dry anomaly. The dry anomaly is centred to the south of the MC, though is spread over Java and adjacent seas, due to pre-existing dry air advected from the east. The mid-level circulation anomaly is tilted northwest–southeast, with moist anomalies either side of the dry anomaly of similar tilt. The days following day 0 are associated with dissipation of upper level anomalies near the Tropics, with propagation of anomalies further to the east (Figure 6d). These anomalies lead to a new stream of anomalous dry air passing over Australia. Dry air originally near to the MC spreads out longitudinally, and the moist anomaly has propagated further east.

1477870x, 2024, 759, Downloaded from https://rmets.onlinelibrary.wiley.com/doi/10.1002/qj.4618 by Test, Wiley Online Library on [21/03/2024]. See the Terms and Conditions (https://onlinelibrary.wiley.com/terms-and-conditions) on Wiley Online Library for rules of use; OA articles are governed by the applicable Creative Commons License

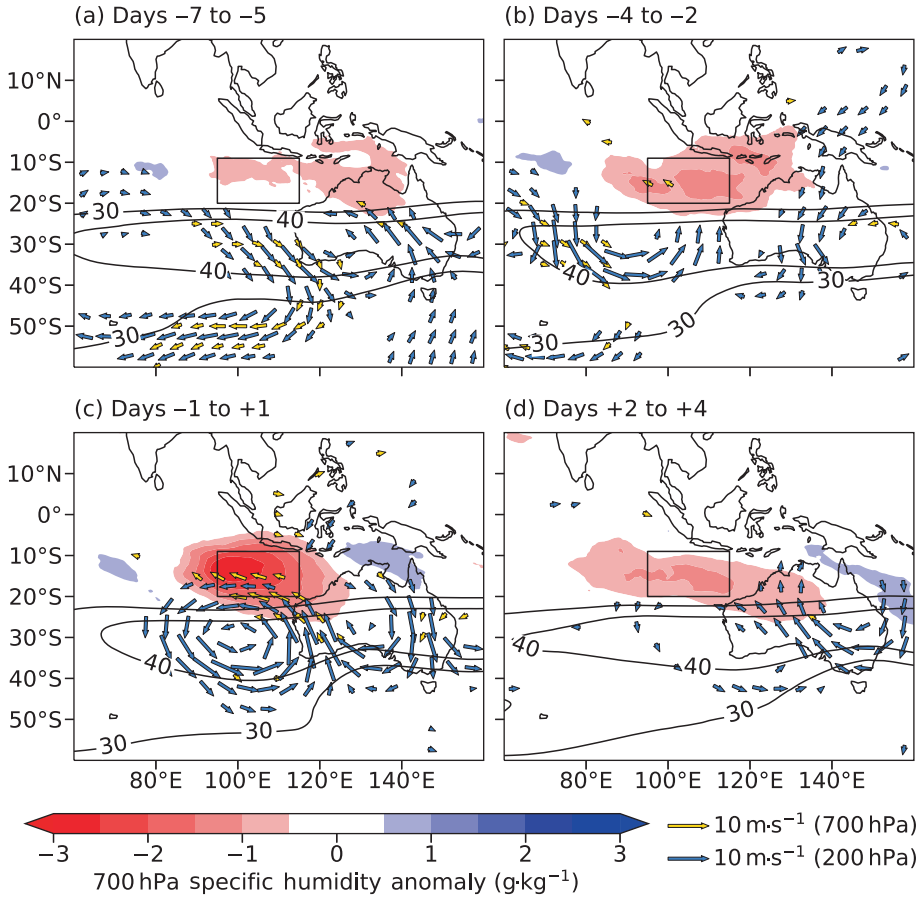

FIGURE 6 As in Figure 5, but for the 56 dry events identified in June–August.

In both DJF and JJA, circulation anomalies at both upper levels and mid-levels are observed. Figure 7 shows time–longitude cross-sections of geopotential height for days −7 to 0, for both the upper level extratropics and mid-level near-Tropics (identifier box region) for both seasons. The choice of these boxes at these levels are in line with the geographical positions of upper and mid-level circulation anomalies noted in Figures 5 and 6. In DJF, cyclonic anomalies prior to the peak of the dry event are associated with an upper level trough in the extratropics, which is strongest at day −3 (Figure 7a). Descent accompanies the southerly advection of dry air to the west of the trough. Anomalies at the mid-levels can also be linked to a persistent mid-level ridge and trough (Figure 7b). Though the ridge does not significantly intensify over time, the trough deepens around day −3. On the other hand, the prevalent extratropical anticyclonic anomaly in JJA is attributed to an upper level ridge (Figure 7c). In contrast to DJF, the mid-level trough is not observed to be more intense than the ridge to the west (Figure 7d). Anomalies of descent accompany the southeasterly advection to the east of the ridge.

The results here show that upper level disturbances within the subtropical jet, developing around 5 days prior to the dry event peak, are a key precursor to dry event occurrence in both seasons. These disturbances drive descent of dry air towards the Tropics. In addition, enhancement in mid-level cyclonic circulation centred over northwestern Australia strengthens mid-level southerlies in DJF, enabling advection of dry air towards the MC. This circulation also produces anomalous southern MC westerlies that advect dry air eastward. On the other hand, in JJA, an enhancement in mid-level anticyclonic circulation just to the west of Australia strengthens mid-level southerlies, though directing dry air to the same region as in DJF. This circulation, too, enhances easterlies south of the MC, which advects dry air westward towards the Indian Ocean. For both seasons, these dry events can therefore be associated with DAIs. Gradual weakening of enhanced wind circulations in DJF and JJA lead to eventual dissipation of the dry anomalies. In both seasons, moist anomalies are observed to the east of the intrusion, tilted in a direction paralleling the trajectory of dry air.

3.3 | Association with modes of variability

The previous section established anomalous circulations unique to DJF and JJA that acted as key regulatory

1477870x, 2024, 759, Downloaded from https://rmets.onlinelibrary.wiley.com/doi/10.1002/qj.4618 by Test, Wiley Online Library on [21/03/2024]. See the Terms and Conditions (https://onlinelibrary.wiley.com/terms-and-conditions) on Wiley Online Library for rules of use; OA articles are governed by the applicable Creative Commons License

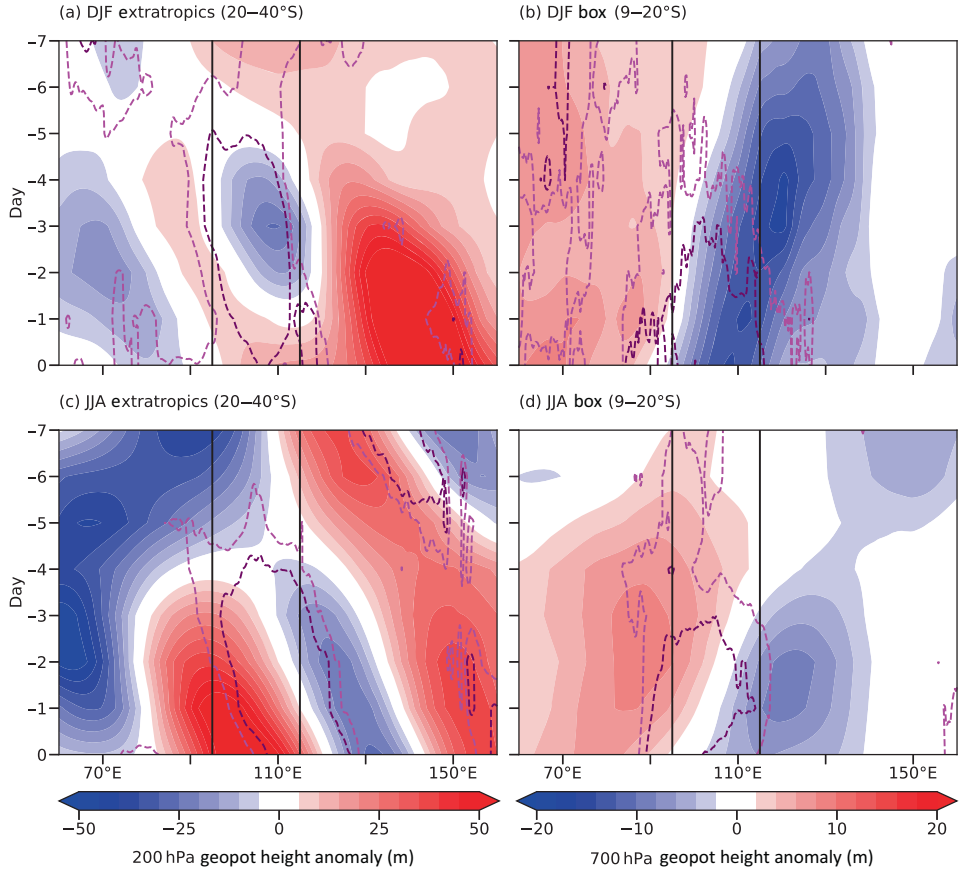

FIGURE 7 (a, b) Hovmöller plots of 200 hPa and 700 hPa geopotential height anomalies from days −7 to 0 for the 47 dry events identified in December–February (DJF) from 1979–80 to 2020–21. Anomalies at 200 hPa are averaged over 20°–40° S, and anomalies at 700 hPa are averaged over 9°–20° S. (c, d) As in (a, b), except for the 56 dry events identified in June–August (JJA). Solid lines represent the longitudinal limits of the identifier box as in Figure 2. For panels (a) and (c), paler and darker dashed contours represent 0.005 Pa·s^{-1} and 0.010 Pa·s^{-1} vertical velocity anomalies respectively, indicating regions of descent. The dashed contours in panels (b) and (d) represent 0.010 Pa·s^{-1} and 0.020 Pa·s^{-1} vertical velocity anomalies respectively.

mechanisms to the onset of a dry event. These circulations could be due to the state of the large-scale environment as modulated by modes of variability.

To investigate this possible link, the dry events in DJF and JJA were grouped into their associations with the state of ENSO, IOD, and MJO, as shown in Table 2 under columns labelled "Frequency". These values were converted to ratios as described in Section 2.4, with results shown in columns labelled "Ratio".

No statistically significant associations between dry events and the state of ENSO or IOD in either season are found. The MJO, on the other hand, shows statistically significant links with dry events in each season. In DJF, the MJO is significantly more (nearly twice as) likely to be in phases 8 and 1, and significantly (nearly four times) less likely to be in phases 2 and 3 when there is a dry event. In JJA, the MJO is significantly more likely to be in phases 2 and 3 and phases 4 and 5, and signficantly (two times) less likely to be in phases 8 and 1 when a dry event occurs. Following the associations between geographical location and MJO phase as in Wheeler and Hendon (2004), the MJO active envelope is more likely to be away from (near to) the MC when a dry event occurs in DJF (JJA), and vice versa. Therefore, there appears to be seasonal differences in associations between phase of the MJO and dry event occurrence.

3.4 | Impact on rainfall

In this section, we analyse the impact of decreased mid-level humidity on regional rainfall patterns. We use the dry events that take place in the available GPM data record from 2000–01 to 2019–20 as GPM does not go as far back as ERA5. This subset provides 25 and 27 dry events for DJF and JJA respectively. Precipitation anomalies associated with each event are composited by lag time and then normalised with respect to the mean rainfall rate at that grid point per season (Figure 1b,c).

During DJF dry events, negative rainfall anomalies develop over the northwest of Australia, up to 6–10 days before the peak of the dry event (Figure 8a). The rainfall anomalies become larger and more widespread, aligning with the negative specific humidity anomalies between days −5 to −2 (Figure 8b). Positive anomalies in normalised precipitation rate are observed to the east over and offshore of the northwest Australian coastline. Around day 0, positive rainfall anomalies dissipate, but continued northward propagation of dry air coincides with decreases in rainfall, with strongest reductions at the core of the dry anomaly, south of Java (Figure 8c). Anomalies south of the MC dissipate and disperse after the dry event peak. These are now more prevalent further west towards the Indian Ocean (Figure 8d). Slight negative rainfall anomalies are

1477870x, 2024, 759, Downloaded from https://rmets.onlinelibrary.wiley.com/doi/10.1002/qj.4618 by Test, Wiley Online Library on [21/03/2024]. See the Terms and Conditions (https://onlinelibrary.wiley.com/terms-and-conditions) on Wiley Online Library for rules of use; OA articles are governed by the applicable Creative Commons License

TABLE 2 Dry event frequency ("Frequency") for both December–February (DJF) and June–August (JJA) across the states of each mode of variability analysed.

Mode	State	DJF (Frequency)	DJF (Ratio)	JJA (Frequency)	JJA (Ratio)
ENSO	El Niño	16	1.04	12	1.08
	Neutral	15	0.94	31	0.94
	La Niña	16	1.02	13	1.08
IOD	Positive	2	1.79	10	1.25
	Neutral	45	1.01	43	0.98
	Negative	0	0.00	3	0.75
MJO	Phase 0	14	0.87	24	0.99
	P2 and P3	2	**0.2**	12	**1.41**
	P4 and P5	7	0.90	8	**1.25**
	P6 and P7	13	1.29	7	1.04
	P8 and P1	11	**1.98**	5	**0.50**

Note: Provided are ratios indicating event frequencies compared with the number of days within each season associated with each state of each mode ('Ratio') as described in Section 2.4. Percentiles of these ratios are obtained by comparison with the distribution of 1,000 bootstrapped samples, also described in Section 2.4. Where these percentiles are below the 5th percentile or above the 95th percentile, ratios are highlighted in bold. MJO phases are associated with geographical locations as follows: phases 2 and 3 (Indian Ocean), phases 4 and 5 (Maritime Continent), phases 6 and 7 (West Pacific), phases 8 and 1 (Western Hemisphere and Africa), as per Wheeler and Hendon (2004). Phase 0 represents times when the MJO amplitude is <1 and therefore weak.
Abbreviations: ENSO, El Niño–Southern Oscillation; IOD, Indian Ocean Dipole; MJO, Madden–Julian Oscillation.

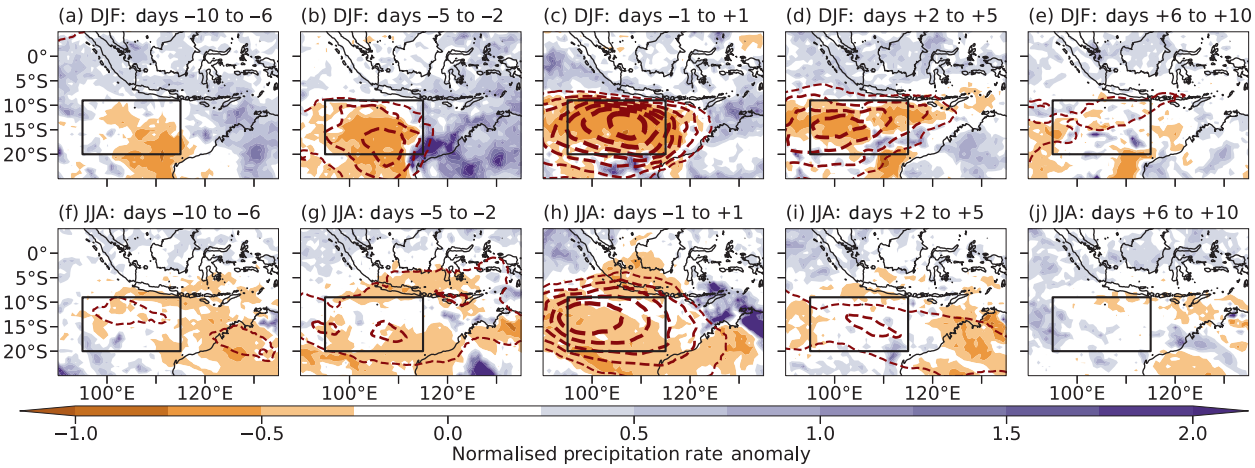

FIGURE 8 Normalised precipitation rate anomalies with respect to the mean rainfall per grid point for dry events in (a–e) December–February (DJF) and (f-j) June–August (JJA) within the available GPM record from 2000–01 to 2019–20 (25 for DJF and 27 for JJA), for days −10 to +10. Anomalies have been binned into sets of days, with smaller bins closer to day 0, which each set of data is averaged over. Dashed contours represent negative specific humidity anomalies averaged over these events, where increases in contour thickness reflect decreases (becoming more negative) in the mean specific humidity anomaly by 0.5 $g \cdot kg^{-1}$, starting at −0.5 $g \cdot kg^{-1}$. The black box represents the domain used for identifying dry events as in Figure 2.

observed over the Lesser Sundas and the neighbouring Flores and Banda seas to the northeast (Figure 1a). Between days +6 and +10, most of the negative rainfall and humidity anomalies have dissipated, though more localised dry air and reduced rainfall signatures persist (Figure 8e).

For JJA dry events, there are pre-existing anomalies of reduced rainfall across the region up to prior to the dry event peak (Figure 8f,g). Rainfall reductions are noted over Java, the Lesser Sundas, south Sulawesi, and the Java and Flores seas (Figure 1a). Only 2–5 days prior to the dry event peak are anomalies originating from the south observed, along with negative specific humidity anomalies, just to the northwest of Australia. Increases in rainfall are noted to the east over Australia. Widespread reductions in rainfall, coinciding with the humidity anomalies, are observed

1477870x, 2024, 759, Downloaded from https://rmets.onlinelibrary.wiley.com/doi/10.1002/qj.4618 by Test, Wiley Online Library on [21/03/2024]. See the Terms and Conditions (https://onlinelibrary.wiley.com/terms-and-conditions) on Wiley Online Library for rules of use; OA articles are governed by the applicable Creative Commons License

around day 0 (Figure 8h). The pre-existing anomaly from the east leads to reductions over the southern MC. The rainfall anomaly from the south shifts northwest towards the Indian Ocean with the reductions in humidity. Positive rainfall anomalies develop to the east of the dry anomaly over the Lesser Sundas and northern Australia, with a northwest–southeast tilt. Both negative and positive rainfall anomalies dissipate over the region up to 5 days after the dry event peak (Figure 8i). Some anomalies shift westward and southeast towards Australia, where there are further reductions in rainfall, matching the trajectory of the humidity anomalies. After day +6, observed anomalies dissipate (Figure 8j).

4 | DISCUSSION

Using the results obtained in Sections 3.1–3.4, we present the mechanisms controlling dry event occurrence and their impacts on rainfall in the southern MC schematically in Figure 9a,b for DJF and JJA.

Analysis of parcel trajectories and precursor anomalies showed that air parcels associated with dry events can be attributed to DAIs, originating from upper level disturbances along the subtropical jet. These processes are likely to be related to Rossby wave breaking, as indicated by similar upper level wind anomaly patterns shown in past studies (e.g., Numaguti, 1995). Parallels can also be drawn in terms of dry air sourcing and pathways leading up to a dry event, as seen in Feng et al. (2021). This work extends Feng et al. (2021)'s observations across a longer time period of analysis for more events.

Negative humidity anomalies observed coming from the east in JJA up to 7 days prior to the peak of the dry event may be attributed to the greater frequency of austral wintertime DAIs (e.g., Casey et al., 2009). Figure 2a highlighted a high-variance region in mid-level specific humidity between New Guinea and Australia. This region may be where the pre-existing dry air originates from, which reaches the MC prior to the intrusions analysed originating from the south over the Indian Ocean in JJA.

There are visible differences, however, in terms of the mechanisms regulating the occurrence of dry events in each season. First, air parcels associated with DAIs take less time to arrive into the Tropics in JJA compared with DJF, and those found in the domain up to 15 days prior to the dry event peak are located within more equatorial latitudes in JJA than in DJF. This observation is likely to be a product of the northward migration of the subtropical jet and intertropical convergence zone ('climatologically wet region') during the austral winter (as depicted in Figure 9b compared with Figure 9a), as well as strengthening of the jet stream, leading to faster advection of air parcels. However, not all points within the box are dry even when a dry event occurs. Therefore, trajectories starting in the Tropics tend to be those not associated with the dry event itself.

Second, shifting of the jet northward in JJA is likely to be altering the direction of dry air trajectories into the MC from southerly to southeasterly, with changes to geopotential height anomalies noted. Past studies have found links between jet characteristics and resultant trajectories of DAIs (e.g., Homeyer & Bowman, 2013). However, the observed trough in DJF and ridge in JJA (dotted circles in Figure 9) may be a result of the events that have been composited. The eventual northwest–southeast tilt attributed to the mid-level trough anomalies in the region of the dry anomaly around day 0 is expected due to refraction of mid-latitude wave trains towards the Tropics (e.g., van der Wiel et al., 2015).

Third, the most pronounced differences between DJF and JJA are in forward trajectories associated with dry events themselves. DJF air parcels have greater re-ascent after the dry event peak (shown as fading arrows in Figure 9a), compared with that in JJA. In addition, JJA air parcels are advected towards the Indian Ocean, with some further northeast from this position up to mainland southeast Asia, compared with DJF, where there is dominantly eastward advection towards New Guinea and some advection westward towards the Indian Ocean. The first association is that the lower level (850 hPa) climatological wind field, provided in Figure 1b, characteristic of the monsoon circulation in each season, suggests mean westerly motion in the lower levels in DJF across the southern-central MC, with easterlies slightly further south, while still within the box latitudes (up to 20° S). The lower level monsoon circulation explains the largely eastward propagation of air parcels in DJF after continued descent below 700 hPa. Figure 1c, on the other hand, shows the opposing monsoon circulation for JJA, where there are strong low-level mean easterlies across the southern MC, which would explain the largely westward advection of parcels. To the northwest of the MC into the Indian Ocean near to the Bay of Bengal and mainland southeast Asia, the low-level monsoon circulation reverses from northeasterly (as in DJF) to southwesterly, providing reasoning for eventual advection of air parcels towards the mainland. Therefore, parcels that continue descent after the peak of the dry event will likely be entrained in the mean monsoon low-level circulation, influencing their eventual trajectory.

Impacts on rainfall generally follow the trajectories presented in Figures 3 and 4. In both seasons, dry air coming from the extratropics suppresses rainfall over the sea in the identifier box, in agreement with results from campaigns such as TOGA COARE over the tropical west

1477870x, 2024, 759, Downloaded from https://rmets.onlinelibrary.wiley.com/doi/10.1002/qj.4618 by Test, Wiley Online Library on [21/03/2024]. See the Terms and Conditions (https://onlinelibrary.wiley.com/terms-and-conditions) on Wiley Online Library for rules of use; OA articles are governed by the applicable Creative Commons License

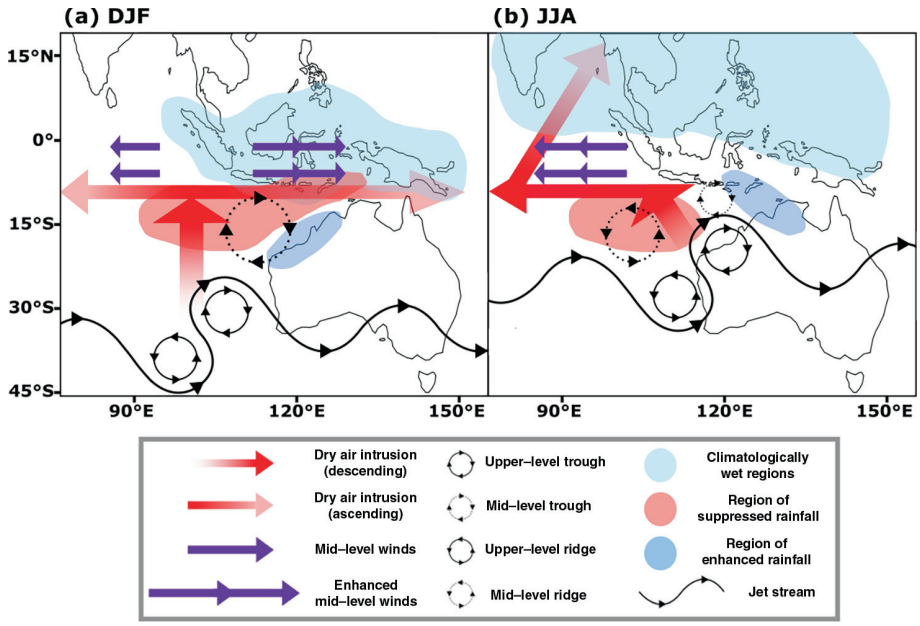

FIGURE 9 Schematic showing the mechanisms regulating the occurrence of dry events, due to extratropical mid-level dry air intrusions, to the south of the Maritime Continent, and their impacts on Maritime Continent rainfall, for (a) December–February (DJF) and (b) June–August (JJA). Arrow size is not representative of intrusion characteristics, merely representing direction and vertical motion.

Pacific (e.g., Parsons et al., 2000). In DJF, dry air propagates eastward, resulting in a suppressed rainfall signal over the Lesser Sundas of Indonesia, and neighbouring seas after the dry event. In JJA, rainfall reductions over the islands of the MC are linked to the pre-existing dry air originating from the east. As JJA trajectories are largely (north)westward, no further reductions over the MC can be attributed to the dry events studied, though rainfall suppression is apparent going into the eastern Indian Ocean.

An increase in rainfall to the east of the dry anomalies, which have a tilt paralleling that of the dry air trajectory itself, was also observed. When analysing key mechanisms regulating dry events, there was flow to the extratropics at both mid-levels and upper levels to the east of troughs, resulting in increases in mid-level specific humidity. Such moist anomalies are found in similar positions to observed positive rainfall anomalies over northwestern and northern Australia, as well as the Lesser Sundas, implying that roughly around day 0 it is possible to get increases in rainfall just to the east. Berry and Reeder (2016) observed similar positive rainfall anomalies, where Australian summertime monsoon bursts took place to the east of an upper level trough. Allen et al. (2009) note similar increases in tropical convection in this region and were able to attribute it more directly to the leading edge of a descending dry air mass from the extratropics. Several researchers have associated amplification of upper level troughs with enhanced convection at the edges and to the east of descending dry air masses elsewhere, thereby steering convection (e.g., Tompkins, 2001; Pohl et al., 2009; de Vries et al., 2016). DAIs and the associated disturbances themselves are driving the flow of moist air necessary to form convection, observed in past studies such as Knippertz (2007) and Ward et al. (2021) over Africa.

Our investigation into associations between dry events and large-scale modes of variability (Table 2) found no significant link between dry event occurrence and both the phases of ENSO and the IOD. Berry and Reeder (2016), for example, also found no significant link between upper level troughs (which regulate Australian summertime monsoon bursts) near to the study region and ENSO. Pohl et al. (2009) found the opposite results for southern Africa, suggestive of global variability in associations between upper level disturbances and the large-scale modes of variability.

In contrast with ENSO and IOD, significant links with the MJO have been noted. For DJF, it was observed that the MJO active phase is significantly more likely to be in phases 8 and 1 and less likely to be in phases 2 and 3 when a dry event occurs. For JJA, when a dry event occurs, the active phase is significantly more likely to be in phases 2 to 5 and less likely during phases 8 and 1. In more condensed terms, when a dry event occurs, the MJO active phase is significantly more likely to be in the vicinity of the MC during JJA and less likely during DJF. The opposite is noted when the MJO active phase is away from the region. Therefore, we find similar results to Berry and Reeder (2016) for DJF (JJA was not examined in their work).

We hypothesise that the link between MJO phase and dry event occurrence is due to circulation anomalies that are driven by the large-scale tropical environment, most dominantly regulated by the MJO on intraseasonal time-scales (Madden & Julian, 1971; Madden & Julian, 1972; Madden & Julian, 1994), which may be a

1477870x, 2024, 759, Downloaded from https://rmets.onlinelibrary.wiley.com/doi/10.1002/qj.4618 by Test, Wiley Online Library on [21/03/2024]. See the Terms and Conditions (https://onlinelibrary.wiley.com/terms-and-conditions) on Wiley Online Library for rules of use; OA articles are governed by the applicable Creative Commons License

product of equatorial wave theory associated with MJO dynamics (e.g., Hendon & Salby, 1994; Maloney & Hartmann, 1998; Matthews, 2000). During the active phase, a tongue of low pressure strengthens to the east, associated with a Kelvin wave, with pressure troughs to the northwest and southwest, associated with Rossby waves (Gill, 1980; Matsuno, 1966). The opposite is observed for the suppressed phase of the MJO. The potential for DAI trajectories to be modified by Rossby waves has in the past been researched over the Indian Ocean in the Dynamics of the MJO field campaign (Chen et al., 2016; Kerns & Chen, 2014). Their observations included a strong MJO event and DAIs over the Indian Ocean. A noted interaction linked DAIs to westward-propagating synoptic Rossby gyres in the active envelope. These gyres induced low-level wind circulations drawing the dry air eastward into the equatorial region west of the envelope, contributing to a 1- to 2-day break in the rainfall during the MJO active phase, favouring a transition to the suppressed phase. This interaction was validated in various simulations (Kuznetsova et al., 2019; Wang et al., 2015).

Mid-level westerly anomalies persist over the southern MC in DJF (double arrows in Figure 9a), linked to the enhanced negative geopotential height anomaly and cyclonic circulation over northwestern Australia. With the strengthened mid-level trough in DJF enhancing both descent of dry air from upper levels and equatorward and eastward advection, a similar interaction to that in Kerns and Chen (2014) may be taking place. When the active phase of the MJO is away from the MC, westward-propagating cyclonic circulations, originating from the active envelope, may enhance westerly flow near to the region of study. In the opposite phases, with reversals of anomalous vortices associated with the MJO, there may be easterly intensification, which is the reason for such air parcels propagating westward (Figure 9a). In JJA, opposite anomalies are noted (Figure 9b), though mid-level easterlies are not as persistent as the westerlies observed in DJF, likely linked to the anomalous geopotential signature being weaker. With dry events more likely when the active phase of the MJO is to the west or over the MC, mid-level ridges (or anticyclonic circulations) are to have greater prevalence near to the region linked with the suppressed phase of the MJO being further to the east. There may be easterly intensification towards the Indian Ocean due to the anticyclonic circulation characteristic of these ridges. Therefore, MJO phase may exert a control on both mid-level circulation and geopotential characteristics noted in each season, potentially interacting with DAIs. Deeper exploration of such associations, however, are beyond the scope of this study and would require further research.

5 | CONCLUSIONS

We have investigated the occurrence of dry events south of the MC and underlying mechanisms in observations for DJF and JJA. Air parcels associated with dry events in both seasons originate from the extratropics in the southern Indian Ocean, as shown by back trajectory analysis, 5–10 days prior to the peak of the dry event. These air parcels are associated with synoptic mid-level DAIs regulated by amplification of upper level disturbances along the subtropical jet up to 5 days before the dry event peak. Descent of dry air takes place to the west of the upper level trough and east of the ridge. DJF intrusions are dominated by southerly mid-level advection and a mid-level cyclonic circulation anomaly (trough) northwest of Australia, whereas JJA intrusions have slight southeasterly flow of dry air from the extratropics due to a mid-level anticyclonic circulation anomaly (ridge) northwest of Australia. The circulation anomaly in DJF enhances westerlies in the southern MC, allowing advection further east. In contrast, the anomaly in JJA enhances easterlies to the west, enabling westward advection. There are interactions between the low-level monsoon circulation in JJA, where northeasterly flow in DJF near mainland southeast Asia and the Bay of Bengal reverses to southwesterly, directing air parcels further northward. Opposing tropical–extratropical flow to the east of intrusions in both seasons transports moisture over Australia and the Lesser Sundas. Though, in both seasons, DAIs descend from around 10 days before the peak of the event to 10 days after, there is eventual re-ascent of air parcels in DJF, with more prolonged low-level flow in JJA. Transport mechanisms, influenced by circulation and geopotential anomalies, attributable to DAI occurrence may be linked to the MJO.

Dry air originating from the extratropics suppresses rainfall, supporting work from other studies analysing convective suppression in the Tropics linked to DAIs. Rainfall suppression signatures largely follow intrusion trajectories, where reduced rainfall may be found in DJF in the southern MC over the Lesser Sundas and neighbouring seas, following the eastward propagation. JJA, on the other hand, has limited rainfall reductions over the southern MC linked to the intrusions analysed. Instead, DAIs originating from further east lead to reductions over Java, Sumatra, southern Borneo, and neighbouring seas. Anomalies linked to the intrusion propagate to the Indian Ocean. In both cases, reduced rainfall can be seen developing around 5 days prior to up to 5 days after the dry event peak. In addition, signatures of positive rainfall anomalies are found to the east of the dry anomalies, indicative of enhanced convection linked to convergence of moist air coming from the Tropics to the extratropics encountering the eastward

1477870x, 2024, 759, Downloaded from https://rmets.onlinelibrary.wiley.com/doi/10.1002/qj.4618 by Test, Wiley Online Library on [21/03/2024]. See the Terms and Conditions (https://onlinelibrary.wiley.com/terms-and-conditions) on Wiley Online Library for rules of use; OA articles are governed by the applicable Creative Commons License

propagation of upper level disturbances and the negative humidity anomalies. These have been observed elsewhere in the Tropics.

This work has extended past work, through usage of 42 years of data compared with select days to weeks in other studies, which were limited by the constraints of observations. However, our approach requires further validation from case study analysis of events linked to DAIs. Such validation is necessary particularly because of the limitations of sample size in terms of number of dry events per season, identified using the method employed. More events are required to provide confirmation of statistically significant links between dry events and the precursor mechanisms, processes that modulate their trajectories, and also their impacts on rainfall. All three of these links are potentially more visible on finer time-scales, so will need further analysis beyond what has been achieved here. Case study analysis will reveal the finer details on what controls dry event occurrence and impacts on convection and rainfall over the MC. Future work may also involve repeating the analysis presented, but for other regions of the MC.

Impacts originating from both the abrupt pauses in convection, enabling recharge in boundary-layer moisture, and also enhanced rainfall/steering of convection on margins through dynamical uplift and low-level interactions, are critical to understand. Future work should involve incorporation of both reanalysis and model data, as this will allow testing of the representation of synoptic processes such as DAIs in global and regional simulations, while increasing our understanding of the associated mechanisms particularly over the MC. These include interactions with the climatological mean circulation, as well as potentially large-scale modes of variability. Precise details on the influence of the MJO and whether it influences circulation and geopotential anomalies regulating DAIs were not covered in this research and would require filtering of the MJO signal in relation to these events. Interactions between DAIs and background modes of variability, however, may vary across the MC, as the modes exert different controls on meteorology based on geographical location. Therefore, more generalised assumptions on their interactions over the whole of the MC cannot be made based on what was learnt from studying the southern portion of the region.

Regardless, our work has provided insight into key processes and impacts linked to DAIs (in terms of both rainfall suppression and enhancement), supporting and expanding on past studies. Improving our general understanding of MC precipitation patterns will provide benefits for forecasting and issuing severe weather warnings, as well as validation of numerical weather prediction models. Any improvements to regional systematic biases and our understanding of more complex processes will also ultimately contribute to improved situational awareness for local agencies, decision-makers, and communities.

AUTHOR CONTRIBUTIONS

Ashar A. Aslam: conceptualization; data curation; formal analysis; investigation; methodology; software; validation; visualization; writing – original draft; writing – review and editing. **Juliane Schwendike:** conceptualization; funding acquisition; methodology; project administration; resources; supervision; validation; writing – review and editing. **Simon C. Peatman:** conceptualization; data curation; funding acquisition; methodology; resources; software; supervision; validation; writing – review and editing. **Cathryn E. Birch:** conceptualization; data curation; funding acquisition; methodology; resources; supervision; validation; writing – review and editing. **Massimo A. Bollasina:** conceptualization; funding acquisition; methodology; resources; supervision; validation; writing – review and editing. **Paul Barrett:** conceptualization; funding acquisition; methodology; resources; supervision; validation; writing – review and editing.

ACKNOWLEDGEMENTS

We wish to thank John Marsham, Amanda Maycock, and researchers involved in the TerraMaris project for their input. We also wish to thank the reviewers for their constructive feedback on our manuscript. ERA5 data were obtained from the Copernicus Climate Data Store through https://cds.climate.copernicus.eu. GPM rainfall data were available as a preprocessed product that had used the IMERG V06 algorithm (Huffman et al., 2020), as highlighted in Section 2. Monthly ENSO ONI data were made available through the NOAA National Weather Service Climate Prediction Center's website through https://origin.cpc.ncep.noaa.gov. Monthly IOD DMI data were accessed through the NOAA Earth System Research Laboratories Physical Sciences Laboratory's website at https://psl.noaa.gov. Daily MJO RMM data, as per the methodology of Wheeler and Hendon (2004), were downloaded from http://www.bom.gov.au/climate/mjo.

ORCID

Ashar A. Aslam https://orcid.org/0000-0003-1362-0842
Simon C. Peatman https://orcid.org/0000-0002-2511-7649
Paul Barrett https://orcid.org/0000-0002-3763-0909

REFERENCES

Allen, G., Vaughan, G., Brunner, D., May, P.T., Heyes, W., Minnis, P. et al. (2009) Modulation of tropical convection by breaking

1477870x, 2024, 759, Downloaded from https://rmets.onlinelibrary.wiley.com/doi/10.1002/qj.4618 by Test, Wiley Online Library on [21/03/2024]. See the Terms and Conditions (https://onlinelibrary.wiley.com/terms-and-conditions) on Wiley Online Library for rules of use; OA articles are governed by the applicable Creative Commons License

Rossby waves. *Quarterly Journal of the Royal Meteorological Society*, 135, 125–137.
Appenzeller, C. & Davies, H. (1992) Structure of stratospheric intrusions into the troposphere. *Nature*, 358, 570–572.
Berry, G.J. & Reeder, M.J. (2016) The dynamics of Australian monsoon bursts. *Journal of the Atmospheric Sciences*, 73, 55–69.
Birch, C.E., Webster, S., Peatman, S.C., Parker, D.J., Matthews, A.J., Li, Y. et al. (2016) Scale interactions between the MJO and the western maritime continent. *Journal of Climate*, 29, 2471–2492.
Bithell, M., Gray, L.J. & Cox, B.D. (1999) A three-dimensional view of the evolution of midlatitude stratospheric intrusions. *Journal of the Atmospheric Sciences*, 56, 673–688.
Brown, R.G. & Zhang, C. (1997) Variability of Midtropospheric moisture and its effect on cloud-top height distribution during TOGA COARE. *Journal of the Atmospheric Sciences*, 54, 2760–2774.
Browning, K.A. (1997) The dry intrusion perspective of extra-tropical cyclone development. *Meteorological Applications*, 4, 317–324.
Casey, S.P.F., Dessler, A.E. & Schumacher, C. (2009) Five-year climatology of Midtroposphere dry air layers in warm Tropical Ocean regions as viewed by AIRS/aqua. *Journal of Applied Meteorology and Climatology*, 48, 1831–1842.
Chen, S.S., Kerns, B.W., Guy, N., Jorgensen, D.P., Delanoë, J., Viltard, N. et al. (2016) Aircraft observations of dry air, the ITCZ, convective cloud systems, and cold pools in MJO during DYNAMO. *Bulletin of the American Meteorological Society*, 97, 405–423.
Danielsen, E.F. (1968) Stratospheric-tropospheric exchange based on radioactivity, ozone and potential vorticity. *Journal of the Atmospheric Sciences*, 25, 502–518.
de Vries, A.J., Feldstein, S.B., Riemer, M., Tyrlis, E., Sprenger, M., Baumgart, M. et al. (2016) Dynamics of tropical-extratropical interactions and extreme precipitation events in Saudi Arabia in autumn, winter and spring. *Quarterly Journal of the Royal Meteorological Society*, 142, 1862–1880.
de Vries, A.J., Ouwersloot, H.G., Feldstein, S.B., Riemer, M., Kenawy, A.M.E., McCabe, M.F. et al. (2018) Identification of tropical-extratropical interactions and extreme precipitation events in the Middle East based on potential vorticity and moisture transport. *Journal of Geophysical Research: Atmospheres*, 123, 861–881.
Draxler, R.R., Spring, S., Maryland, U.S.A. & Hess, G.D. (1998) An overview of the HYSPLIT_4 modelling system for trajectories, dispersion, and deposition. *Australian Meteorological Magazine*, 47, 295–308.
Feng, L., Zhang, T., Koh, T.Y. & Hill, E.M. (2021) Selected years of monsoon variations and extratropical dry-air intrusions compared with the Sumatran GPS Array observations in Indonesia. *Journal of the Meteorological Society of Japan*, 99, 505–536.
Ferrett, S., Yang, G.Y., Woolnough, S.J., Methven, J., Hodges, K. & Holloway, C.E. (2020) Linking extreme precipitation in Southeast Asia to equatorial waves. *Quarterly Journal of the Royal Meteorological Society*, 146, 665–684.
Fletcher, J.K., Parker, D.J., Hunt, K.M., Vishwanathan, G. & Govindankutty, M. (2018) The interaction of Indian monsoon depressions with northwesterly midlevel dry intrusions. *Monthly Weather Review*, 146, 679–693.
Fletcher, J.K., Parker, D.J., Turner, A.G., Menon, A., Martin, G.M., Birch, C.E. et al. (2020) The dynamic and thermodynamic structure of the monsoon over southern India: new observations from the INCOMPASS IOP. *Quarterly Journal of the Royal Meteorological Society*, 146, 2867–2890.
Funatsu, B.M. & Waugh, D.W. (2008) Connections between potential vorticity intrusions and convection in the eastern tropical Pacific. *Journal of the Atmospheric Sciences*, 65, 987–1002.
Gill, A. (1980) Some simple solutions for heat-induced tropical circulation. *Quarterly Journal of the Royal Meteorological Society*, 106, 447–462.
Haylock, M. & McBride, J. (2001) Spatial coherence and predictability of Indonesian wet season rainfall. *Journal of Climate*, 14, 3882–3887.
Hendon, H.H. & Salby, M.L. (1994) The life cycle of the Madden–Julian oscillation. *American Meteorological Society*, 51, 2225–2237.
Hersbach, H., Bell, B., Berrisford, P., Hirahara, S., Horányi, A., Muñoz-Sabater, J. et al. (2020) The ERA5 global reanalysis. *Quarterly Journal of the Royal Meteorological Society*, 146, 1999–2049.
Homeyer, C.R. & Bowman, K.P. (2013) Rossby wave breaking and transport between the tropics and extratropics above the subtropical jet. *Journal of the Atmospheric Sciences*, 70, 607–626.
Huffman, G.J., Bolvin, D.T., Braithwaite, D., Hsu, K., Joyce, R., Kidd, C. et al. (2020) Nasa Global Precipitation Measurement (GPM) Integrated Multi-satellitE Retrievals for GPM (IMERG): Algorithm Theoretical Basis Document (ATBD) Version 06. https://gpm.nasa.gov/sites/default/files/document_files/IMERG_ATBD_V06.pdf
Ichikawa, H. & Yasunari, T. (2006) Time-space characteristics of diurnal rainfall over Borneo and surrounding oceans as observed by TRMM-PR. *Journal of Climate*, 19, 1238–1260.
Jin, F. & Hoskins, B.J. (1995) The direct response to tropical heating in a Baroclinic atmosphere. *Journal of the Atmospheric Sciences*, 52, 307–319.
Johnson, R.H., Ciesielski, P.E. & Cotturone, J.A. (2001) Multiscale variability of the atmospheric mixed layer over the Western Pacific warm Pool. *Journal of the Atmospheric Sciences*, 58, 2729–2750.
Kerns, B.W. & Chen, S.S. (2014) Equatorial dry air intrusion and related synoptic variability in MJO initiation during DYNAMO. *Monthly Weather Review*, 142, 1326–1343.
Knippertz, P. (2007) Tropical-extratropical interactions related to upper-level troughs at low latitudes. *Dynamics of Atmospheres and Oceans*, 43, 36–62.
Kumar, K.N., Phanikumar, D.V., Sharma, S., Basha, G., Naja, M., Ouarda, T.B. et al. (2019) Influence of tropical-extratropical interactions on the dynamics of extreme rainfall event: a case study from Indian region. *Dynamics of Atmospheres and Oceans*, 85, 28–40.
Kuznetsova, D., Dauhut, T. & Chaboureau, J.P. (2019) The three atmospheric circulations over the Indian Ocean and the maritime continent and their modulation by the passage of the MJO. *Journal of the Atmospheric Sciences*, 76, 517–531.
Lucas, C. & Zipser, E.J. (2000) Environmental variability during TOGA COARE. *Journal of the Atmospheric Sciences*, 57, 2333–2350.
Lucas, C., Zipser, E.J. & Ferrier, B.S. (2000) Sensitivity of tropical West Pacific oceanic squall lines to tropospheric wind and moisture profiles. *Journal of the Atmospheric Sciences*, 57, 2351–2373.
Madden, R.A. & Julian, P.R. (1971) Detection of a 40–50 day oscillation in the zonal wind in the tropical Pacific. *Journal of the Atmospheric Sciences*, 28, 702–708.
Madden, R.A. & Julian, P.R. (1972) Description of global-scale circulation cells in the tropics with a 40–50 day period. *Journal of the Atmospheric Sciences*, 29, 1109–1123.

1477870x, 2024, 759, Downloaded from https://rmets.onlinelibrary.wiley.com/doi/10.1002/qj.4618 by Test, Wiley Online Library on [21/03/2024]. See the Terms and Conditions (https://onlinelibrary.wiley.com/terms-and-conditions) on Wiley Online Library for rules of use; OA articles are governed by the applicable Creative Commons License

Madden, R.A. & Julian, P.R. (1994) Observations of the 40–50-day tropical oscillation — a review. *Monthly Weather Review*, 122, 814–837.

Maloney, E.D. & Hartmann, D.L. (1998) Frictional moisture convergence in a composite life cycle of the Madden-julian oscillation. *Journal of Climate*, 11, 2387–2403.

Mapes, B.E. & Zuidema, P. (1996) Radiative-dynamical consequences of dry tongues in the tropical troposphere. *Journal of the Atmospheric Sciences*, 53, 620–638.

Matsuno, T. (1966) Quasi-geostrophic motions in the equatorial area*. *Journal of the Meteorological Society of Japan*, 44, 25–43.

Matthews, A.J. (2000) Propagation mechanisms for the Madden-Julian oscillation. *Quarterly Journal of the Royal Meteorological Society*, 126, 2637–2651.

Mori, S., Hamada, J.-I., Yamanaka, M.D., Okamoto, N., Murata, F., Sakurai, N. et al. (2004) Diurnal Land-Sea rainfall peak migration over Sumatera Island, Indonesian maritime continent, observed by TRMM satellite and intensive Rawinsonde soundings. *Monthly Weather Review*, 132, 2021–2039.

Murata, F., Yamanaka, M.D., Mori, S., Kudsy, M., Sribimawati, T. & Suhardi, B. (2006) Dry intrusions following eastward-propagating synoptic-scale cloud systems over Sumatera Island. *Journal of the Meteorological Society of Japan*, 84, 277–294.

Narulita, I. & Ningrum, W. (2018) Extreme flood event analysis in Indonesia based on rainfall intensity and recharge capacity. *IOP Conference Series: Earth and Environmental Science*, 118, 12045.

Neale, R. & Slingo, J. (2003) The maritime continent and its role in the global climate: a GCM study. *Journal of Climate*, 16, 834–848.

NOAA. (2019) El Niño regions. https://www.cpc.ncep.noaa.gov/products/analysis_monitoring/ensostuff/nino_regions.shtml

Numaguti, A. (1995) Characteristics of 4-to-20-day-period disturbances observed in the equatorial Pacific during the TOGA COARE IOP. *Journal of the Meteorological Society of Japan*, 73, 353–377.

Parker, D.J., Willetts, P., Birch, C., Turner, A.G., Marsham, J.H., Taylor, C.M. et al. (2016) The interaction of moist convection and mid-level dry air in the advance of the onset of the Indian monsoon. *Quarterly Journal of the Royal Meteorological Society*, 142, 2256–2272.

Parsons, D.B., Yoneyama, K. & Redelsperger, J.-L. (2000) The evolution of the tropical western Pacific atmosphere-ocean system following the arrival of a dry intrusion. *Quarterly Journal of the Royal Meteorological Society*, 126, 517–548.

Peatman, S.C., Matthews, A.J. & Stevens, D.P. (2014) Propagation of the Madden-Julian oscillation through the maritime continent and scale interaction with the diurnal cycle of precipitation. *Quarterly Journal of the Royal Meteorological Society*, 140, 814–825.

Peatman, S.C., Schwendike, J., Birch, C.E., Marsham, J.H., Matthews, A.J. & Yang, G.-Y. (2021) A local-to-large scale view of maritime continent rainfall: control by ENSO, MJO and equatorial waves. *Journal of Climate*, 34, 8933–8953.

Pohl, B., Fauchereau, N., Richard, Y., Rouault, M. & Reason, C.J. (2009) Interactions between synoptic, intraseasonal and interannual convective variability over southern Africa. *Climate Dynamics*, 33, 1033–1050.

Qian, J.H. (2008) Why precipitation is mostly concentrated over islands in the maritime continent. *Journal of the Atmospheric Sciences*, 65, 1428–1441.

Ramage, C.S. (1968) Role of a tropical "maritime continent" in the atmospheric circulation. *Monthly Weather Review*, 96, 365–370.

Rauniyar, S.P. & Walsh, K.J. (2013) Influence of ENSO on the diurnal cycle of rainfall over the maritime continent and Australia. *Journal of Climate*, 26, 1304–1321.

Raveh-Rubin, S. (2017) Dry intrusions: Lagrangian climatology and dynamical impact on the planetary boundary layer. *Journal of Climate*, 30, 6661–6682.

Redelsperger, J.-L., Parsons, D.B. & Guichard, F. (2002) Recovery processes and factors limiting cloud-top height following the arrival of a dry intrusion observed during TOGA COARE. *Journal of the Atmospheric Sciences*, 59, 2438–2457.

Rodwell, M.J. (1997) Breaks in the Asian monsoon: the influence of southern hemisphere weather systems. *Journal of the Atmospheric Sciences*, 54, 2597–2611.

Ryoo, J.-M., Waugh, D.W. & Gettelman, A. (2008) Variability of subtropical upper tropospheric humidity. *Atmospheric Chemistry and Physics*, 8, 2643–2655.

Saji, N., Goswami, B., Vinayachandran, P. & Yamagata, T. (1999) A dipole mode in the tropical Indian Ocean. *Nature*, 401, 360–363.

Saji, N. & Yamagata, T. (2003) Possible impacts of Indian Ocean dipole mode events on global climate. *Climate Research*, 25, 151–169.

Seto, T.H., Yamamoto, M.K., Hashiguchi, H., Fukao, S., Abo, M., Kozu, T. et al. (2006) Observational study on westerly wind burst over Sumatra, Indonesia by the equatorial atmosphere radar-a case study during the first CPEA campaign. *Journal of the Meteorological Society of Japan*, 84A, 95–112.

Silverman, V., Nahum, S. & Raveh-Rubin, S. (2021) Predicting origins of coherent air mass trajectories using a neural network—the case of dry intrusions. *Meteorological Applications*, 28, 1–18.

Stohl, A. (2001) A 1-year Lagrangian "climatology" of airstreams in the northern hemisphere troposphere and lowermost stratosphere. *Journal of Geophysical Research Atmospheres*, 106, 7263–7279.

Tompkins, A.M. (2001) Organization of Tropical Convection in low vertical wind shears: the role of water vapor. *Journal of the Atmospheric Sciences*, 58, 529–545.

van der Wiel, K., Matthews, A.J., Stevens, D.P. & Joshi, M.M. (2015) A dynamical framework for the origin of the diagonal South Pacific and South Atlantic convergence zones. *Quarterly Journal of the Royal Meteorological Society*, 141, 1997–2010.

Vaughan, G., Antonescu, B., Schultz, D.M. & Dearden, C. (2017) Invigoration and capping of a convective rainband ahead of a potential vorticity anomaly. *Monthly Weather Review*, 145, 2093–2117.

Vincent, C.L. & Lane, T.P. (2016) Evolution of the diurnal precipitation cycle with the passage of a Madden-Julian oscillation event through the maritime continent. *Monthly Weather Review*, 144, 1983–2005.

Volonté, A., Turner, A.G. & Menon, A. (2020) Airmass analysis of the processes driving the progression of the Indian summer monsoon. *Quarterly Journal of the Royal Meteorological Society*, 146, 2949–2980.

Wang, S., Sobel, A.H., Zhang, F., Sun, Y.Q., Yue, Y. & Zhou, L. (2015) Regional simulation of the October and November MJO events observed during the CINDY/DYNAMO field campaign at Gray zone resolution. *Journal of Climate*, 28, 2097–2119.

1477870x, 2024, 759, Downloaded from https://rmets.onlinelibrary.wiley.com/doi/10.1002/qj.4618 by Test, Wiley Online Library on [21/03/2024]. See the Terms and Conditions (https://onlinelibrary.wiley.com/terms-and-conditions) on Wiley Online Library for rules of use; OA articles are governed by the applicable Creative Commons License

Ward, N., Fink, A.H., Keane, R.J., Guichard, F., Marsham, J.H., Parker, D.J. et al. (2021) Synoptic timescale linkage between mid-latitude winter troughs Sahara temperature patterns and northern Congo rainfall: a building block of regional climate variability. *International Journal of Climatology*, 41, 3153–3173.

Waugh, D.W. & Polvani, L.M. (2000) Climatology of intrusions into the tropical upper troposphere. *Geophysical Research Letters*, 27, 3857–3860.

Wernli, H. & Davies, H.C. (1997) A Lagrangian-based analysis of extratropical cyclones. I: the method and some applications. *Quarterly Journal of the Royal Meteorological Society*, 123, 467–489.

Wheeler, M. & Kiladis, G.N. (1999) Convectively coupled equatorial waves: analysis of clouds and temperature in the wavenumber-frequency domain. *Journal of the Atmospheric Sciences*, 56, 374–399.

Wheeler, M.C. & Hendon, H.H. (2004) An all-season real-time multivariate MJO index: development of an index for monitoring and prediction. *Monthly Weather Review*, 132, 1917–1932.

Wijayanti, P., Zhu, X., Hellegers, P., Budiyono, Y. & van Ierland, E.C. (2017) Estimation of river flood damages in Jakarta, Indonesia. *Natural Hazards*, 86, 1059–1079.

Yamanaka, M.D., Ogino, S.Y., Wu, P.M., Hamada, J.-I., Mori, S., Matsumoto, J. et al. (2018) Maritime continent coastlines controlling Earth's climate. *Progress in Earth and Planetary Science*, 5, 1–28.

Yang, G.-Y., Hoskins, B. & Slingo, J. (2003) Convectively coupled equatorial waves: a new methodology for identifying wave structures in observational data. *Journal of the Atmospheric Sciences*, 60, 1637–1654.

Yang, G.-Y. & Slingo, J. (2001) The diurnal cycle in the tropics. *Monthly Weather Review*, 129, 784–801.

Yang, S., Cui, X. & Ran, L. (2009) Analyses of dry intrusion and instability during a heavy rainfall event that occurred in northern China. *Atmospheric and Oceanic Science Letters*, 2, 108–112.

Yokoi, S., Mori, S., Katsumata, M., Geng, B., Yasunaga, K., Syamsudin, F. et al. (2017) Diurnal cycle of precipitation observed in the western coastal area of Sumatra Island: offshore preconditioning by gravity waves. *Monthly Weather Review*, 145, 3745–3761.

Yoneyama, K. & Fujitani, T. (1995) The behavior of dry westerly air associated with convection observed during the TOGA-COARE R/V Natsushima cruise. *Journal of the Meteorological Society of Japan*, 73, 291–304.

Yoneyama, K. & Parsons, D.B. (1999) A proposed mechanism for the intrusion of dry air into the tropical Western Pacific region. *Journal of the Atmospheric Sciences*, 56, 1524–1546.

Zhang, C. & Chou, M.-D. (1999) Variability of water vapor, infrared radiative cooling, and atmospheric instability for deep convection in the equatorial Western Pacific. *Journal of the Atmospheric Sciences*, 56, 711–723.

How to cite this article: Aslam, A.A., Schwendike, J., Peatman, S.C., Birch, C.E., Bollasina, M.A. & Barrett, P. (2024) Mid-level dry air intrusions over the southern Maritime Continent. *Quarterly Journal of the Royal Meteorological Society*, 150(759), 727–745. Available from: https://doi.org/10.1002/qj.4618

1477870x, 2024, 759, Downloaded from https://rmets.onlinelibrary.wiley.com/doi/10.1002/qj.4618 by Test, Wiley Online Library on [21/03/2024]. See the Terms and Conditions (https://onlinelibrary.wiley.com/terms-and-conditions) on Wiley Online Library for rules of use; OA articles are governed by the applicable Creative Commons License